

# In situ growth of 2D metal-organic framework ion sieve interphase for reversible zinc anodes

Jing SUN<sup>1</sup>, Qinping Jian<sup>1</sup>, Bin Liu<sup>1</sup>, Pengzhu Lin<sup>1</sup>, and T.S. Zhao<sup>2</sup>

<sup>1</sup>The Hong Kong University of Science and Technology

<sup>2</sup>Hong Kong University of Science and Technology School of Engineering

April 25, 2024

## Abstract

Zinc metal anodes are gaining popularity in aqueous electrochemical energy storage systems for their high safety, cost-effectiveness, and high capacity. However, the service life of zinc metal anodes is severely constrained by critical challenges, including dendrites, water-induced hydrogen evolution, and passivation. In this study, a protective two-dimensional metal-organic framework interphase is in situ constructed on the zinc anode surface with a novel gel vapor deposition method. The ultrathin interphase layer ( $\sim 1 \mu\text{m}$ ) is made of layer-stacking 2D nanosheets with angstrom-level pores of around  $2.1 \text{ \AA}$ , which serves as an ion sieve to reject large solvent-ion pairs while homogenizes the transport of partially desolvated zinc ions, contributing to a uniform and highly reversible zinc deposition. With the shielding of the interphase layer, an ultra-stable zinc plating/stripping is achieved in symmetric cells with cycling over 1000 h at  $0.5 \text{ mA cm}^{-2}$  and  $\sim 700 \text{ h}$  at  $1 \text{ mA cm}^{-2}$ , far exceeding that of the bare zinc anodes (250 and 70 h). Furthermore, as a proof-of-concept demonstration, the full cell paired with  $\text{MnO}_2$  cathode demonstrates improved rate performances and stable cycling (1200 cycles at  $1 \text{ A g}^{-1}$ ). This work provides fresh insights into interphase design to promote the performance of zinc metal anodes.

## Introduction

Zinc metal is a highly promising anode material for aqueous electrochemical energy storage systems due to its high theoretical capacity ( $820 \text{ mAh g}^{-1}$  and  $5855 \text{ mAh cm}^{-3}$ ) [1], natural abundance, and excellent safety profile [2]. However, the rampant zinc dendrite growth and parasitic side reactions lead to the short service time of the aqueous zinc batteries, which has significantly limited their practical application [3]. During the zinc electrodeposition, non-uniform zinc ion transport and accumulation of the "tip effect" lead to the formation of highly porous flake-like zinc dendrites, which can penetrate the separator and result in an internal short circuit [4]. Meanwhile, solvated  $\text{Zn}^{2+}$  ions, typically in the form of  $[\text{Zn}(\text{H}_2\text{O})_6]^{2+}$ , undergo desolvation in the electric double layer before reaching the zinc surface and receiving electrons to be reduced to Zn. The desolvated water molecule is more prone to decomposition, resulting in parasitic hydrogen evolution reactions (HER) and zinc corrosion [5]. Therefore, it is urgently needed to search for effective strategies for addressing these abovementioned issues. Various strategies have been proposed to circumvent challenges encountered by zinc anodes, including electrode design [6], interfacial modification [7], and electrolyte design [8]. Interfacial modification is regarded as one of the most promising ways to improve the Zn anode performance, as the electrode-electrolyte interface plays a crucial role in ion transport and electrochemical reactions.

Various electron-conductive or insulating materials with different functions and mechanisms have been successfully adopted to form protective layers on the Zn surface. Electron-conductive materials include carbon material [9], which can easily incorporate different functional groups and interact with  $\text{Zn}^{2+}$ , and metal [10] or alloys [11], which can provide abundant and uniform nucleation sites and exhibit low nucleation barriers. However, zinc deposits on top of the electron-conducting layer may eventually develop into dendrites and penetrate the membrane. Electron-insulating materials, including a series of insulating polymers [12] that

exhibit excellent mechanical properties and functional groups, can constrain the zinc dendrite growth and guide the diffusion of  $\text{Zn}^{2+}$  ions, and inorganic materials (e.g.,  $\text{CaCO}_3$  [13],  $\text{TiO}_2$  [14],  $\text{ZrO}_2$  [15], etc.), which are typically synthesized *ex situ* and coated on the zinc surface with binders to form a porous layer with binders can avoid the direct contact of zinc and aqueous electrolyte and uniformize the  $\text{Zn}^{2+}$  flux. However, the characteristics of zinc deposition with various coating layers vary due to large deviations in the particle size of inorganic materials.

Among various coating materials, metal-organic frameworks (MOFs) representing a class of electron-insulating materials with ordered and tunable pore sizes have been *ex situ* or *in situ* coated on the zinc surface to suppress dendrite growth [16]. For example, ZIF-8 [17], UiO-66 [18], and functionalized MOFs such as UiO-66-(COOH)<sub>2</sub> have been *ex situ* coated and serve as ion-conductive layers that promote the zinc ion desolvation and  $\text{Zn}^{2+}$  diffusion [19]. Zhou et al. constructed a super-saturated electrolyte front surface by coating pre-synthesized ZIF-7 particles with polyvinylidene fluoride (PVDF) binder on the zinc surface. The channel size of ZIF-7 is smaller than that of water-solvated  $\text{Zn}^{2+}$  ions, which enables the MOF layer to reject large-size solvated ion complexes and promote the desolvation of  $\text{Zn}^{2+}$  ions [20]. Despite the demonstrated effects in extending the lifespan of zinc anode, the *ex situ* coating inevitably involves polymer binders, which leads to a large thickness, sacrificed energy density, and unclear underlying mechanisms of MOF functions.

To overcome this limitation, there have been works to *in situ* synthesize binder-free MOF layers and provide critical discussions on the size effect of the MOF channels and the crystallization of the MOF materials. To be specific, binder-free layers composed of MOFs such as ZIF-L [21], ZIF-8 [22], ZSB (Zn-stp-by) [23], Zn-TCPP [24], and MOFs derived by the coordination between  $\text{Zn}^{2+}$  and  $[\text{Fe}(\text{CN})_6]^{3-}$  [25] are *in situ* grown on zinc anode surface. These layers with functional groups can interact with  $\text{Zn}^{2+}$  and their ordered nanochannels can homogenize  $\text{Zn}^{2+}$  flux. In addition to these *in situ* grown crystalline MOF layers, Xiang et al. constructed a continuous amorphous ZIF-8 MOF layer, which can eliminate the dendrite growth at the grain boundaries in crystalline MOF layer and make the protective functions more extraordinary [26]. Furthermore, Zhou et al. applied a fast current-driven synthesis method to *in situ* grow a crack-free hydrophobic ZIF-7<sub>x-8</sub> layer to promote zinc ion desolvation [27]. Based on the above review, it can be concluded that the *in situ* growth of seamless MOF layers with rationally selected pores and functional groups effectively boosts zinc ion desolvation and suppresses dendrite growth.

Herein, after screening various MOFs,  $\text{Zn}_2(\text{bim})_4$  [28] was selected as a promising coating material for zinc anodes, which has pore sizes of only  $\sim 2.1$  Å. In addition, taking advantage of the 2D structures of  $\text{Zn}_2(\text{bim})_4$ , we innovatively apply the gel vapor deposition (GVD) method to grow the 2D sheet on the zinc surface layer by layer and achieve a dense and connected MOF layer. The *in situ* stacked layer of nanosheet with a fine pore structure can effectively reject the large size of  $[\text{Zn}(\text{H}_2\text{O})_6]^{2+}$  association ( $\sim 8.6$  Å), and only allow the transport of compact  $\text{Zn}^{2+}$  ion pairs, since the diameter of zinc ion is around 1.48 Å [29]. The uniform channels with small pore sizes lead to a homogenized flux of partially desolvated  $\text{Zn}^{2+}$ , as shown in Figure 1, enabling the  $\text{Zn}@Zn_2(\text{bim})_4//\text{Zn}@Zn_2(\text{bim})_4$  symmetric cell to be stably operated for over 1000 h at 0.5 mA cm<sup>-2</sup> and 0.5 mAh cm<sup>-2</sup>, and 700 h at 1 mA cm<sup>-2</sup> and 1 mAh cm<sup>-2</sup>. In addition, the full cell assembled with  $\text{Zn}@Zn_2(\text{bim})_4$  anode and  $\text{MnO}_2$  cathode can be stably cycle for 1200 cycles at 1 A g<sup>-1</sup>.

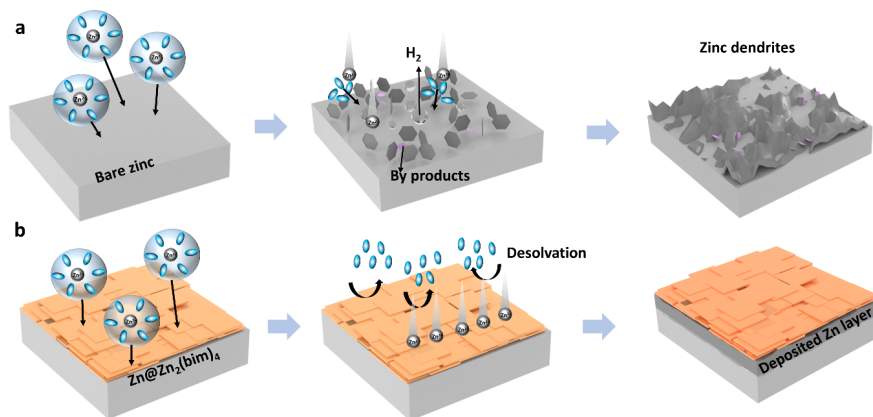


Figure 1. Schematic diagram of (a) dendrite growth and side reactions on bare Zn and (b) regulated desolvation and Zn deposition on  $\text{Zn@Zn}_2(\text{bim})_4$ .

## Results and Discussion

According to Ref. [28],  $\text{Zn}_2(\text{bim})_4$  can be *ex situ* obtained through hydrothermal transformation of 3D zeolitic imidazolate framework ZIF-7, and the layered  $\text{Zn}_2(\text{bim})_4$  can then be exfoliated through a soft-physical process. Later, there have been many trials to *in situ* grow layered  $\text{Zn}_2(\text{bim})_4$  nanosheet on different substrates. For example, Zhang et al. reported a direct growth technique by converting  $\text{ZnO}$  to  $\text{Zn}_2(\text{bim})_4$  membrane with the assistance of ammonia on a porous hollow fiber substrate<sup>[30]</sup>. Recently, the GVD method was reported to *in situ* grow a ZIF-8 membrane on PVDF fibers by Li et al.<sup>[31]</sup> Inspired by this, we apply the GVD method for the first time to *in situ* grow a 2D MOF layer on the zinc surface, as shown in Figure 2a.

Firstly, Zn-based sol was prepared by dissolving zinc acetate dihydrate in ethylene glycol monomethyl ether and ethanolamine. The as-prepared zinc-based sol was then dip-coated on the Zn surface and heat treated to remove the solvent, resulting in the zinc-based gel that was tightly attached to the Zinc surface. As shown in Figure 2a, the Zn-based gel layer serves as the Zn source and oriented growth sites for 2D MOF nanosheets. After interacting with the benzimidazole vapor, the  $\text{Zn}_2(\text{bim})_4$  MOF layer in lamellated structure would *in situ* grow on the zinc surface. It is shown that the  $\text{Zn}_2(\text{bim})_4$  nanosheets grow on the Zn surface with an oriented direction and stack layer by layer (Fig. 2b and e). The thickness of the MOF layer is around 1  $\mu\text{m}$ , and C and Zn are the main elements of the  $\text{Zn}_2(\text{bim})_4$ MOF (Figure 2b-d, and Figure 2e-g). The top view of the  $\text{Zn@Zn}_2(\text{bim})_4$  shows that the oriented 2D MOF nanosheet can form a continuous membrane with almost no slit, which ensures that the zinc ions transport through the pores of MOFs instead of directly passing from the slits. In addition, as discussed in recent work, continuous MOF membranes can avoid the growth of zinc dendrites along the grain boundaries of crystalline MOFs<sup>[26]</sup>. The structure of the 2D nanosheet is characterized by TEM images, as shown in Figure 2h, with Zn, C, and N elements being detected (Figure S1, supporting information). Since the samples for TEM characterization are prepared by scraping the MOF layer from  $\text{Zn@Zn}_2(\text{bim})_4$  samples, more than one layer of the nanosheet is observed in the TEM image. In addition, the scarce N element not detected from the SEM image can be examined from the TEM characterization. Moreover, the surface of  $\text{Zn@Zn}_2(\text{bim})_4$  turns gray as compared to the metallic luster of bare zinc, as shown in Figure 2i. The contact angle test shows that after growing the MOF layer, the surface becomes more hydrophobic, as witnessed by the increase in the contact angle from  $93.7^\circ$  on bare zinc and to  $122.4^\circ$  on  $\text{Zn@Zn}_2(\text{bim})_4$  (Figure 2j and k). The hydrophobic surface is conducive to avoiding the direct contact of water molecules with the Zn surface, thus suppressing water-induced corrosion. The X-ray diffraction (XRD) pattern of the crystal structure of  $\text{Zn}_2(\text{bim})_4$  is determined according to Cambridge Crystallographic Data Centre (CCDC), no. 675375, as depicted in Figure 2l. The peak at  $9^\circ$  corresponds to the (002) plane of  $\text{Zn}_2(\text{bim})_4$  nanosheet, suggesting that the membrane is highly oriented. In contrast to previous methods that used *ex situ* fabricated MOF particles with binders to coat the Zn surface, the *in*

*situ* formed MOF nanosheet layer grows into a continuous membrane. In addition, compared with other *in situ* grown MOF particles, the MOF nanosheet with square shapes stacks layer by layer and forms a tightly connected layer.

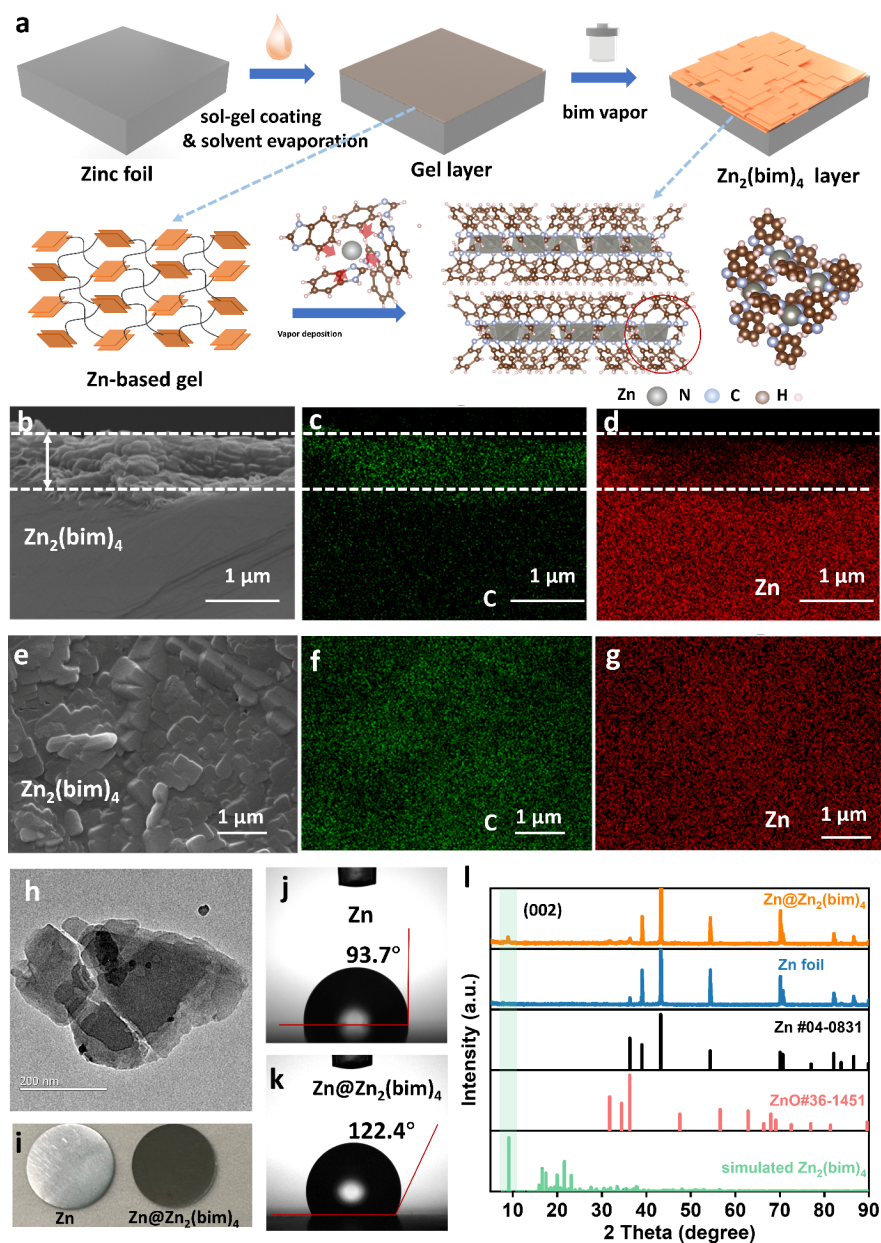


Figure 2. (a) Schematic of the sol-gel coating and GVD method to *in situ* grow the MOF layer. (b)-(l) Morphologies and structure characterization of Zn@Zn<sub>2</sub>(bim)<sub>4</sub>. (b) SEM image, (c)-(d) energy dispersive spectroscopy (EDS) mapping of the cross-section view of Zn@Zn<sub>2</sub>(bim)<sub>4</sub>. (e) SEM image, (f) and (g) EDS mapping of the top view of Zn@Zn<sub>2</sub>(bim)<sub>4</sub>. (h) TEM images nanosheets. (i) Digital photo. Contact angle of water droplet on (j) bare zinc and (k) Zn@Zn<sub>2</sub>(bim)<sub>4</sub>. (l) XRD patterns of bare Zn foil and Zn@Zn<sub>2</sub>(bim)<sub>4</sub>.

Typically, the zinc deposition involves the following steps: i) mass transport of the solvated zinc ion in the bulk electrolyte; ii) desolvation in the electric double layer; iii) charge transfer; and iv) electro-crystallization

(nucleation and growth)<sup>[32]</sup>, as depicted in Figure 3a and b. The overpotential corresponding to each process can be denoted as  $\eta_{\text{mt}}$ ,  $\eta_{\text{rxn}}$ ,  $\eta_{\text{ct}}$ , and  $\eta_{\text{ec}}$ , respectively. Therefore, we investigated the electrochemical properties of  $\text{Zn@Zn}_2(\text{bim})_4$  anode with various techniques from the perspective of the above-mentioned processes.

Firstly, we investigate the impedance of the symmetric cell under different temperatures using EIS. It can be seen from the inset in Figures 3c and d that the ohmic resistance (the first interception of the EIS arc with the  $x$ -axis) of  $\text{Zn@Zn}_2(\text{bim})_4//\text{Zn@Zn}_2(\text{bim})_4$  cell is slightly larger than that of bare zinc cell. The insulating MOF layer with tiny pores form a barrier for zinc ion to transport, which leads to increased ohmic resistance ( $\eta_{\text{mt}}$  in  $\text{Zn@Zn}_2(\text{bim})_4$  cells is higher than that in bare zinc cell). During the desolvation process, a large amount of water in the  $[\text{Zn}(\text{H}_2\text{O})_6]^{2+}$  was physically rejected before the ions could pass through the MOF layer, which can boost the desolvation process at the zinc front surface, as shown in Figure 3b. With the charge transfer resistance at different temperatures determined from EIS tests (Figures 3c and d), the activation energy ( $E_a$ ) of desolvation during  $\text{Zn}^{2+}$  plating can be calculated according to the Arrhenius equation<sup>[33]</sup>:

$$\ln(T/R_{\text{ct}}) = \frac{E_a}{RT} + \ln A(1)$$

Where  $R_{\text{ct}}$ ,  $T$ ,  $R$  and  $A$  represent charge transfer resistance, absolute temperature, standard gas constant, and preexponential constant, respectively. According to the calculation,  $E_a$  of  $\text{Zn}^{2+}$  on  $\text{Zn@Zn}_2(\text{bim})_4$  is 20.6  $\text{kJ mol}^{-1}$ , which is smaller than that on bare Zn surface (29.9  $\text{kJ mol}^{-1}$ ), indicating an enhanced desolvation process (Figure 3e). After that, the nucleation of  $\text{Zn}^{2+}$  ion on bare Cu and  $\text{Cu@Zn}_2(\text{bim})_4$  is characterized through the constant current deposition process in  $\text{Zn}/\text{Cu}$  half cells and the CV test in a three-electrode setup. As shown in Figure 3f, when applying a constant current, the voltage shifts from the equilibrium to  $E_A$ , corresponding to the formation of crystal nuclei. With the the deposition process going on, the voltage reaches a plateau ( $E_B$ ) corresponding to a steady growth process. Previously, the difference ( $\Delta\eta$ ) between  $E_A$  and  $E_B$  is regarded as the nucleation potential. With such theory, the nucleation overpotential on  $\text{Cu@Zn}_2(\text{bim})_4$  is increased compared to bare Cu. However, as discussed in Ref. <sup>[32]</sup>,  $E_A$  instead of  $\Delta\eta$  should be recognized as the nucleation overpotential since  $\Delta\eta$  represents the gap of the driving force between nucleation and growth. With this, the nucleation overpotential on  $\text{Cu@Zn}_2(\text{bim})_4$  is still larger than that on bare zinc, which can further be confirmed from the CV results (Figure S2, supporting information). According to the relationship between the critical Zn nucleus and nucleation overpotential (NOP)<sup>[34]</sup>, the increased NOP indicates a more fine-grained Zn nucleus, favoring the crystallographic orientation of Zn deposits.

Furthermore, we investigated the diffusion mode using chronoamperometry (CA)<sup>[35]</sup>, as shown in Figure 3g. In the bare zinc setup, the current increases gradually, representing a 2D-diffusion mode and a steady increase in the electrochemical active surface area, corresponding to the formation of the porous and nonuniform zinc dendrites. In contrast, the current gradually reaches a plateau on  $\text{Zn@Zn}_2(\text{bim})_4$ , representing the homogeneous and dense deposition of zinc. The corrosion-resistant capability of the in situ grown MOF layer was investigated by linear polarization experiments in 2M  $\text{ZnSO}_4$  solution (Figure 3h). The corrosion potential of the  $\text{Zn@Zn}_2(\text{bim})_4$  is more positive than that of bare Zn, indicating the inhibited tendency of corrosion caused by hydrogen evolution<sup>[36]</sup>. In addition, a lower corrosion current on  $\text{Zn@Zn}_2(\text{bim})_4$  represents a lower corrosion rate<sup>[34]</sup>. To sum up, the dense MOF interphase acts as an ion sieve with ordered fine pores, which increases mass transport overpotential but boosts the desolvation process and prevents water-induced corrosion. With an increased nucleation overpotential, more homogenous and dense zinc deposition can be achieved, suppressing the formation of zinc dendrites.

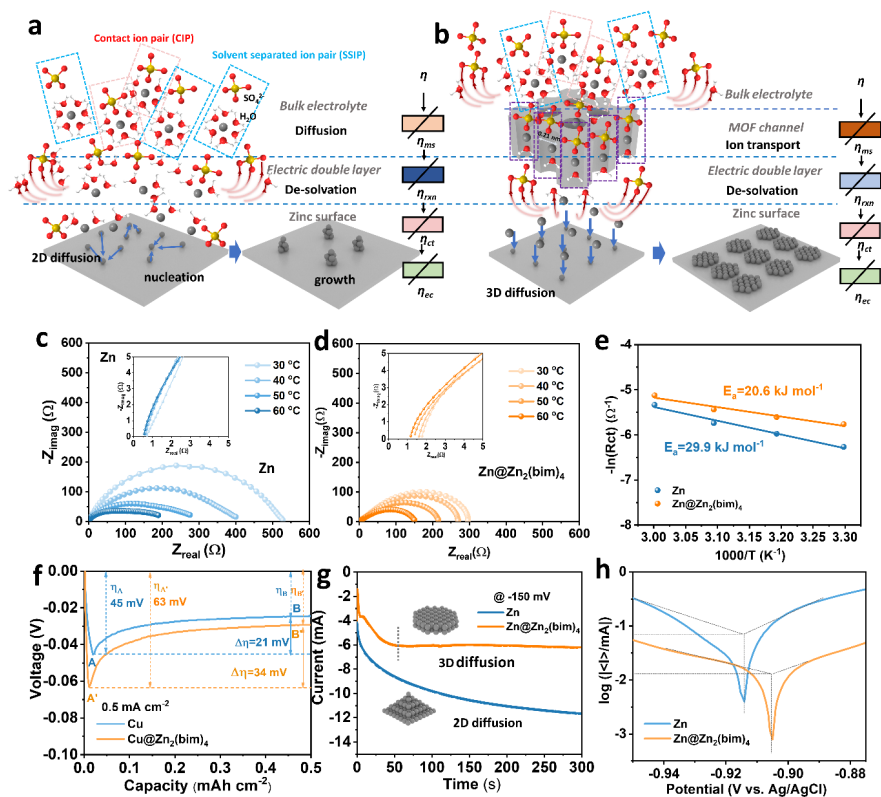


Figure 3. Schematics of zinc electrodeposition on (a) bare Zn and (b)  $\text{Zn}@Zn_2(\text{bim})_4$ . Electrochemical characterization of the  $\text{Zn}@Zn_2(\text{bim})_4$  anode. (c)-(d) EIS profiles of symmetric cells at temperatures from 30-60 . (e) Arrhenius curves. (f) Zinc nucleation on different substrates. (g) Chronoamperometric curves for bare Zn and  $\text{Zn}@Zn_2(\text{bim})_4$ . (h) Potentiodynamic polarization curves.

Then, we characterized the electrochemical performance of the *in situ* growing MOF zinc anodes. Firstly, Zn//Cu asymmetric cells were employed to examine the coulombic efficiency (CE) of Zn plating/stripping with *in situ* MOF interphase. As shown in Figure 4a, Zn//Cu@ $\text{Zn}_2(\text{bim})_4$  exhibits higher steady CE (98.04%) than its counterparts 94.74% for bare Cu at 0.5 mA cm<sup>-2</sup> and 0.5 mAh cm<sup>-2</sup> with an obviously longer cycle life, indicating that the HER is effectively suppressed with the *in situ* MOF layer. The voltage profiles of the zinc depositing and stripping in different cycles (Figure 4b and c) show that the Zn//Cu@ $\text{Zn}_2(\text{bim})_4$  has a larger overpotential, due to the increased mass transport barrier and nucleation potential as discussed earlier.

Furthermore, the cycling stability of Zn anodes was examined with Zn//Zn symmetric cells. The rate performance of the  $\text{Zn}@Zn_2(\text{bim})_4$  symmetric cell shows an increased overpotential compared with the cell with bare zinc, which is consistent with the above-discussed electrochemical tests. With the current density steadily increasing from 0.25 to 5 mA cm<sup>-2</sup> and then returning to 2 mA cm<sup>-2</sup>, the cell can also steadily cycle with an overall time exceeding 500h. However, the bare zinc cell got short-circuited much earlier, even though it returns at a smaller current density of 1 mA cm<sup>-2</sup> (Figure 4d). Then the long-term cyclability of anodes with MOF layer is verified in symmetric cells under galvanostatic cycles. At a current density of 0.5 mA cm<sup>-2</sup> with a capacity of 0.5 mAh cm<sup>-2</sup>, the  $\text{Zn}@Zn_2(\text{bim})_4$  symmetric cell can cycle for over 1000h, while the bare zinc cell suffered from a short circuit after around 250 h (Figure 4e). It is worth noting that the regular fluctuations in the voltage profile are due to temperature changes. Under different testing conditions (1 mA cm<sup>-2</sup> and 1 mAh cm<sup>-2</sup>), the service time of  $\text{Zn}@Zn_2(\text{bim})_4$  symmetric cells reaches 700 h as compared to a lifespan of shorter than 100 h for bare zinc (Figure 4f). It is interesting to note that during cycling, the

overpotential for the  $\text{Zn}@Zn_2(\text{bim})_4$  symmetric cells undergoes an initial increase, followed by a decrease, and then gradually reaches a steady state. When observing the voltage profile in a single stripping and depositing cycle (Figure 4g), we notice that there is a relatively large overpotential for zinc stripping to take place in the 10<sup>th</sup> and 25<sup>th</sup> cycles, and the overpotential also increases towards the end of each cycle. However, as cycling continues, the profiles gradually become flatter. The possible reason for this phenomenon is that the transport of zinc ions in the MOF layer with angstrom-level pores may need to be activated. During the first several cycles of testing, the pathways for zinc ion transport may not be continuous, leading to an increased overpotential. However, after the activation stage, the overpotential returns to a relatively small level.

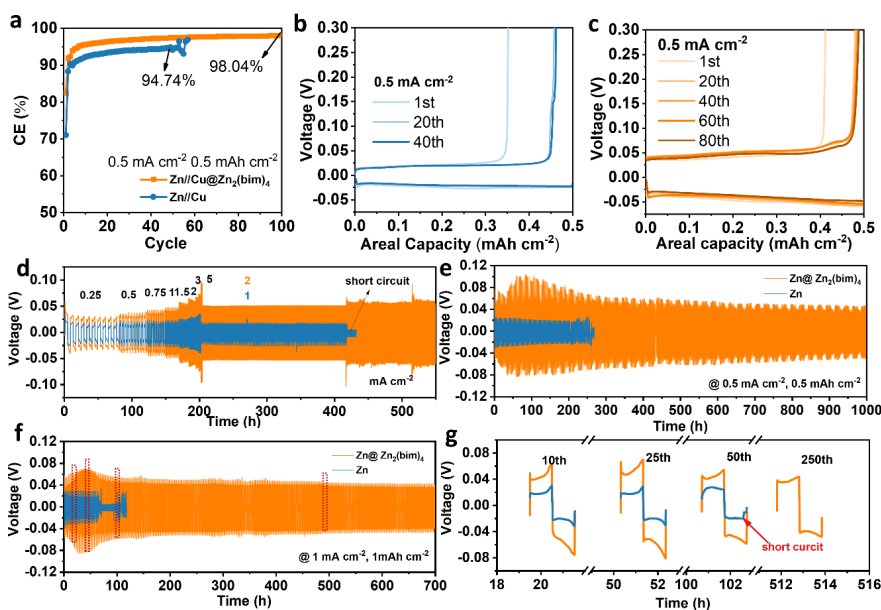


Figure 4.  $\text{Zn//Cu}$  half cell and  $\text{Zn//Zn}$  symmetric cell performance. (a) CE of  $\text{Zn//Cu}$  and  $\text{Zn//Cu}@Zn_2(\text{bim})_4$  Voltage profile of zinc deposition and stripping of (b)  $\text{Zn//Cu}$  and (c)  $\text{Zn//Cu}@Zn_2(\text{bim})_4$  half cells. (d) Rate performance, (e)-(f) cycling performance of the symmetric cell. (g) Selected voltage profile of the  $\text{Zn}@Zn_2(\text{bim})_4//\text{Zn}@Zn_2(\text{bim})_4$  at different cycles.

The effect of angstrom-level channels on the desolvation of  $\text{Zn}^{2+}$  ions is studied with Raman spectroscopy, as shown in Figure 5. Typically, Zn ions are coordinated with water molecules and exist in aqueous solutions as solvent-separated ion pairs (SSIP)  $[\text{Zn}^{2+}(\text{H}_2\text{O})_6\cdot\text{SO}_4^{2-}]$ , which is reflected from Raman peak at around  $931\text{ cm}^{-1}$ , and contact ion pairs (CIP)  $[\text{Zn}^{2+}(\text{H}_2\text{O})_5\cdot\text{OSO}_3^{2-}]$  that appears  $935.5\text{ cm}^{-1}$  [37]. As the concentration of  $\text{ZnSO}_4$  increases, more  $\text{Zn}^{2+}$  ions forms CIPs, as seen in Figure 5a, and the peak of  $\nu\text{-SO}_4^{2-}$  shifts to a higher frequency. The Raman peak of  $\nu\text{-SO}_4^{2-}$  shifts even to a higher frequency in MOF channels, indicating the coordination of  $\text{Zn}^{2+}$  with even fewer water molecule. Thus, the spectral results indicate that the MOF channels with a diameter of  $2.1\text{ \AA}$  only allow for the transport of  $\text{Zn}^{2+}$  in a mono-hydrated coordination type and function as ion sieve interphase with the size screening effect, as schematically shown in Figure 5b.

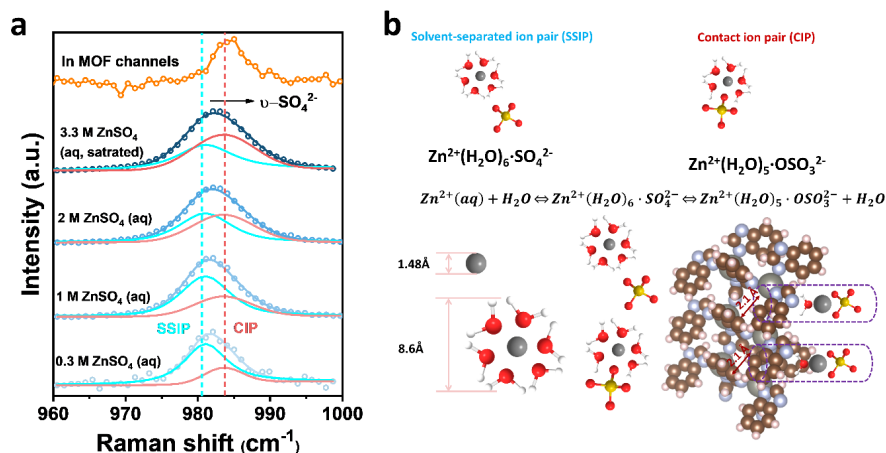


Figure 5. (a) Raman spectra of  $\nu\text{-SO}_4^{2-}$  band of  $\text{ZnSO}_4$  of different concentrations. (b) zinc ion association in MOF channel.

As a proof-of-concept demonstration, the MOF-growing zinc anode was paired with a  $\text{MnO}_2$  cathode (Figure S3, supporting information) to assemble full cells. The  $\text{Zn@Zn}_2(\text{bim})_4/\text{MnO}_2$  cell demonstrated improved rate performance in higher discharge capacities than the cell with bare Zn anode as the current density increased from 0.1 to 2  $\text{A g}^{-1}$  (Figure 6a). Although the discharge capacities of cells with Zn and  $\text{Zn@Zn}_2(\text{bim})_4$  were almost the same at 0.1  $\text{A g}^{-1}$ , the gap between the two cells gradually amplified with an increase in current density. The detailed voltage profiles at 0.5 and 1  $\text{A g}^{-1}$  are shown in Figure 6b. Additionally, the  $\text{Zn@Zn}_2(\text{bim})_4/\text{MnO}_2$  cell exhibited a slightly smaller discharge capacity (115.5  $\text{mAh g}^{-1}$ ) compared to the bare zinc full cell (139.6  $\text{mAh g}^{-1}$ ) but a much more stable cycling performance over 1200 cycles at 1  $\text{A g}^{-1}$ , retaining 48% of the capacity for  $\text{Zn@Zn}_2(\text{bim})_4/\text{MnO}_2$  vs 23% for  $\text{Zn}/\text{MnO}_2$  (Figure 6c). A similar trend is found at a smaller cathode loading (e.g., 1.2  $\text{mg cm}^{-2}$ ) (Figure S4, supporting information). Furthermore, both cells were disassembled after cycling, and the zinc deposition morphology was viewed from both the cross-section and top views. For bare zinc, the zinc deposition was highly porous and stuck to the glass fiber separator, as shown in Figure 6d and f. In contrast, the surface of the  $\text{Zn@Zn}_2(\text{bim})_4$  after cycling was smooth, and the zinc was densely deposited underneath the MOF layer (Figure 6e and g). Therefore, compared to the bare zinc cell, the repeated stripping and depositing of zinc with  $\text{Zn@Zn}_2(\text{bim})_4$  are less likely to pierce the separator, thereby leading to an increased cycle life in symmetric cells.

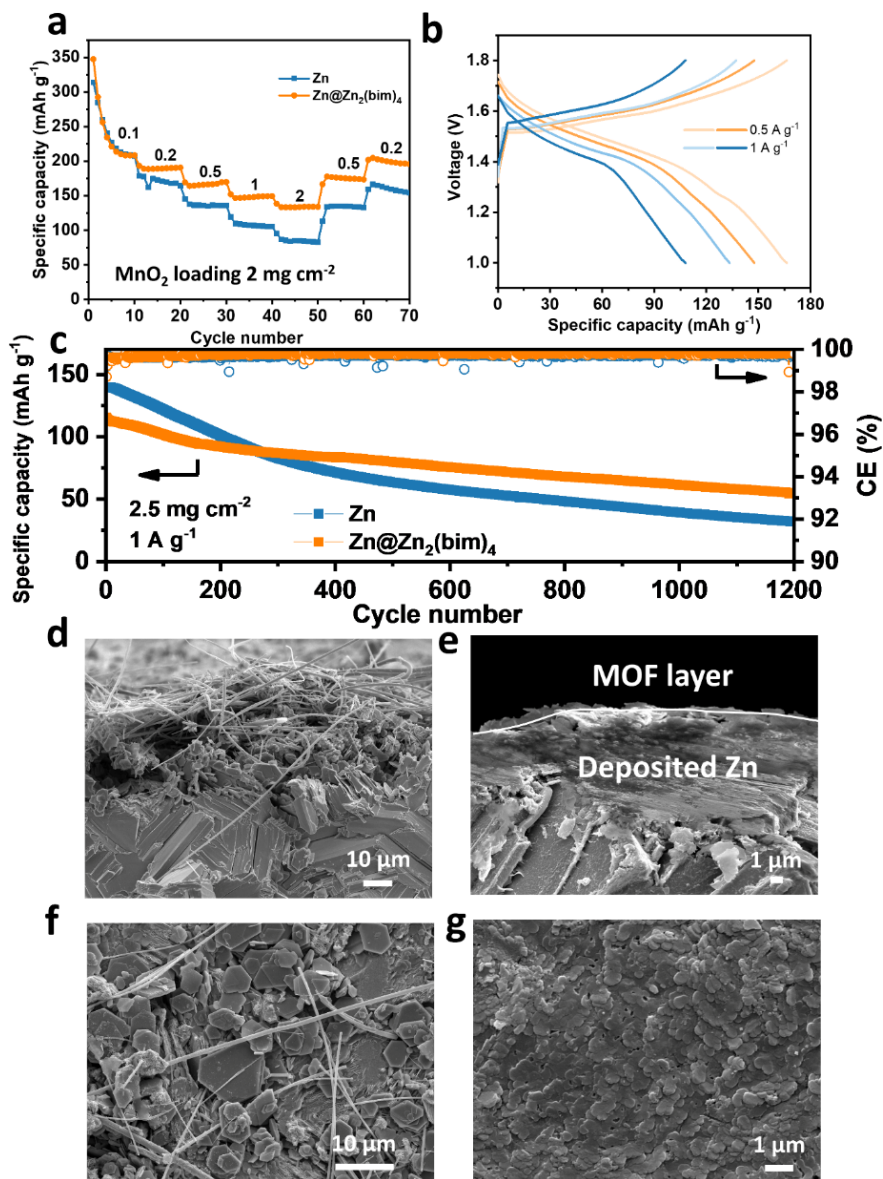


Figure 6. Electrochemical performance of full cells paired with  $\text{MnO}_2$  cathode and post-mortem characterization of Zn surface after cycling. (a) Rate performance, (b) voltage profile, and (c) cycling performance of Zn// $\text{MnO}_2$  and Zn@Zn<sub>2</sub>(bim)<sub>4</sub>// $\text{MnO}_2$  batteries. (d)-(e) Cross section view and (f)-(g) top view of the anode after cycling.

## Conclusion

To summarize, an *in situ* ion sieve interphase based on 2D Zn<sub>2</sub>(bim)<sub>4</sub> MOF with a pore size of  $\sim 2.1$  Å was developed for high-performance zinc anodes using a novel gel vapor deposition method. This MOF protective interphase with fine pores can physically reject the transport of large Zn<sup>2+</sup>-H<sub>2</sub>O coordination pairs and facilitate the desolvation of Zn<sup>2+</sup> at the electrode/electrolyte interface, as evidenced by Raman spectra and impedance analysis. As a result, it significantly extends the lifespan of Zn//Zn symmetric cells ( $\sim 1000$  h at 0.5 mA cm<sup>-2</sup>, 0.5 mAh cm<sup>-2</sup>, and  $\sim 700$  h at 1 mA cm<sup>-2</sup>, 1 mAh cm<sup>-2</sup>). Furthermore, when the Zn@Zn<sub>2</sub>(bim)<sub>4</sub> anode was paired with a MnO<sub>2</sub> cathode, the full cell demonstrated improved rate performance

and stable cycling over 1200 cycles at 1 A g<sup>-1</sup>. The GVD method allows for the *in situ* layered growth of a 2D MOF into a continuous layer, and the unique pore sizes can physically desolvate zinc ions and alleviate water-induced corrosion. This work offers insights into the regulation of Zn<sup>2+</sup> transport with the size effect of MOF channels and provides a route for interface construction to extend the cycle life of zinc anodes.

## Experimental Section

**Materials.** Ethylene glycol monomethyl ether (EGME) was bought from Scharlau. Ethanolamine was obtained from Sigma-Aldrich. Benzimidazole, Zn<sub>2</sub>SO<sub>4</sub>[?]<sub>7</sub>H<sub>2</sub>O, and MnSO<sub>4</sub>[?]<sub>2</sub>H<sub>2</sub>O, polyvinylidene fluoride (PVDF), and N-methylpyrrolidone (NMP) were purchased from was provided by Aladdin. Carboxyl-multiwalled carbon nanotube was bought from Xianfeng nano-materials Co. Ltd.

**Zn-based gel coating.** 1g zinc acetate (Zn(Ac)<sub>2</sub>\*2H<sub>2</sub>O) was dispersed in 12 mL ethylene glycol monomethyl ether (C<sub>3</sub>H<sub>8</sub>O<sub>2</sub>, EGME) and stirred at 60 °C for 0.5 h to get a white suspension. Then, 1 mL ethanolamine was dropwise added to the suspension, and zinc acetate was dissolved to get the transparent Zn-based sol. The solution was aged at room temperature for 10 hours. Zn foil (100 μm) was washed with ethanol and water and then soaked in a dilute H<sub>2</sub>SO<sub>4</sub> solution to remove the extra zinc oxides on the surface. One side of zinc foil was protected by a Kapton tape in the following synthesis process. To form a homogenous Zn-based gel on a Zn foil surface, the zinc-based sol (0.5 mL) was dip-casted onto a 5 cm×5 cm zinc foil surface. After drying at 120 °C in the vacuum oven for 1 h, a uniform gel layer was tightly attached to the zinc foil surface.

**Zn<sub>2</sub>(bim)<sub>4</sub> MOF layer growing.** 0.7g benzimidazole (bim) powder was put in a Teflon-lined stainless steel autoclave, and zinc-based gel-coated zinc foil was cut into 3mm-wide pieces and vertically placed above the powder without contact. The autoclave was heat treated at 185 °C for 12 h for vapor deposition. After natural cooling, the gel was converted to Zn<sub>2</sub>(bim)<sub>4</sub>, and the Zn@Zn<sub>2</sub>(bim)<sub>4</sub> was washed with methanol several times to remove the residual bim on the surface and vacuum-dried. The MOF layer can also be grown on the copper foil (Cu@Zn<sub>2</sub>(bim)<sub>4</sub>) by applying the same method.

**MnO<sub>2</sub>/CNT cathode fabrication.** MnO<sub>2</sub>/CNT nanorods were synthesized according to previously reported work<sup>[12a]</sup>, and the weight fraction of MnO<sub>2</sub> in the MnO<sub>2</sub>/CNT is determined to be ~74% by the thermo gravimetric analysis (TGA) test (Figure S3b, Supporting information). Then, the MnO<sub>2</sub>/CNT, carbon black, and PVDF binder were mixed with a weight ratio of 8:1:1 in NPM solution to form a homogenous ink. The ink was dipped into carbon paper and dried in a vacuum oven for 12 h, and cathodes with different mass loadings can be prepared.

## Material characterization

The morphologies of Zn@Zn<sub>2</sub>(bim)<sub>4</sub> and Zn deposition after cycling were presented by a field-emission scanning electron microscope (FESEM, JEOL 7100F) equipped with energy dispersive spectrometer (EDS, OXFORD X-MAX). The MOF layer was scraped from the *in situ* growth, and its 2D structure was characterized using a TEM (JEOL 2010). The crystal structure of the Zn and MOF layer was analyzed by XRD (PW1825) with Cu K $\alpha$  radiation. The Raman spectra were carried out with the InVia (Renishaw) Raman spectrometer with a 633 nm laser as the excitation source. The Raman for liquid solutions is taken by common procedures. For MOF decorated electrodes, the Zn@Zn<sub>2</sub>(bim)<sub>4</sub> electrodes were cycled in symmetric cells at 0.5 mA cm<sup>-2</sup> and 0.5 mAh 10 times, and the small amount of liquid electrolyte was wiped out using a tissue before taking the Raman test. The excitation light is focused on the electrode surface with a depth of less than 1 μm; the power of the laser beam is adjusted to be 10% of a maximum of 30 mW to avoid damage to the MOF material. The wettability of bare zinc and Zn@Zn<sub>2</sub>(bim)<sub>4</sub> were tested by contact angles measurement (Biolin Theta). The TGA of as-prepared MnO<sub>2</sub>/CNT cathode material was conducted with a thermogravimetric analyzer (Q5000TA) with a heating rate of 5 min<sup>-1</sup> from 20 to 800 under airflow.

## Electrochemical characterization

**Tafel curves:** The Tafel tests were carried out in a three-electrode setup with 2M ZnSO<sub>4</sub> as the electrolyte, Zn or Zn@Zn<sub>2</sub>(bim)<sub>4</sub> as the working electrode, and Ag/AgCl as the reference electrode, and platinum (Pt) mesh as the counter electrode. **Cyclic voltammetry (CV):** The CV tests were carried out in

the same three-electrode setup with Cu or Cu@Zn<sub>2</sub>(bim)<sub>4</sub> as the working electrode. Chronoamperometry (CA): The CA test was also conducted in the three-electrode setup. The working electrode is Zn or Zn@Zn<sub>2</sub>(bim)<sub>4</sub>, and the reference electrode is Zn. The other electrochemical tests were conducted in CR2025 coin cells assembled with a glass fiber separator and 2M ZnSO<sub>4</sub> as the electrolyte. The **electrochemical impedance spectroscopy (EIS)** and **Zn plating/stripping performance** were tested in Zn//Zn or Zn@Zn<sub>2</sub>(bim)<sub>4</sub>//Zn@Zn<sub>2</sub>(bim)<sub>4</sub> symmetric cells. The CE of anodes was measured in Zn//Cu or Zn//Cu@Zn<sub>2</sub>(bim)<sub>4</sub> cells with a current density of 0.5 mA cm<sup>-2</sup> for 1h. The electrochemical performance of full cells (Zn//MnO<sub>2</sub> or Zn@Zn<sub>2</sub>(bim)<sub>4</sub>//MnO<sub>2</sub>) were tested under different current densities with cutoff voltages of 1.0 and 1.8V and 2M Zn<sub>2</sub>SO<sub>4</sub> and 0.2 M MnSO<sub>4</sub> as electrolyte. Tafel curves, CV, CA and EIS were conducted in electrochemical workstation (SP-200, Biologic). The frequency for EIS test ranges from 100 kHz to 10 mHz with an amplified voltage of 10 mV. The Zn plating/stripping performance, CEs of Zn anode, and full cell tests were carried out in battery testing system (Neware).

### Acknowledgements

This work was fully supported by the grants from the Research Grants Council of the Hong Kong Special Administrative Region, China (Project No. C5031-20).

### Conflict of Interest

The authors declare no conflict of interest.

### References

- [1] J. Wang, Y. Yang, Y. Zhang, Y. Li, R. Sun, Z. Wang, H. Wang, *Energy Storage Materials* **2021** , 35, 19.
- [2] P. Ruan, S. Liang, B. Lu, H. J. Fan, J. Zhou, *Angewandte Chemie* **2022** , 134, e202200598.
- [3] S. Wang, Y. Zhao, H. Lv, X. Hu, J. He, C. Zhi, H. Li, *Small* **2023** , 2207664.
- [4] J. Zheng, Z. Huang, Y. Zeng, W. Liu, B. Wei, Z. Qi, Z. Wang, C. Xia, H. Liang, *Nano Letters* **2022** , 22, 1017.
- [5] D. Wang, Q. Li, Y. Zhao, H. Hong, H. Li, Z. Huang, G. Liang, Q. Yang, C. Zhi, *Advanced Energy Materials* **2022** , 12, 2102707.
- [6] a) Q. Jian, Z. Guo, L. Zhang, M. Wu, T. Zhao, *Chemical Engineering Journal* **2021** , 425, 130643; b) Y. Mu, Z. Li, B.-k. Wu, H. Huang, F. Wu, Y. Chu, L. Zou, M. Yang, J. He, L. Ye, *Nature Communications* **2023** , 14, 4205.
- [7] a) Q. Zhang, J. Luan, Y. Tang, X. Ji, H. Wang, *Angewandte Chemie International Edition* **2020** , 59, 13180; b) J. Zheng, Z. Huang, F. Ming, Y. Zeng, B. Wei, Q. Jiang, Z. Qi, Z. Wang, H. Liang, *Small* **2022** , 18, 2200006; c) Z. Zhang, B. Xi, X. Ma, W. Chen, J. Feng, S. Xiong, *SusMat* **2022** , 2, 114.
- [8] a) T. Zhang, Y. Tang, S. Guo, X. Cao, A. Pan, G. Fang, J. Zhou, S. Liang, *Energy & Environmental Science* **2020** , 13, 4625; b) A. Li, J. Li, Y. He, M. Wu, *Journal of Energy Chemistry* **2023** .
- [9] a) C. Shen, X. Li, N. Li, K. Xie, J.-g. Wang, X. Liu, B. Wei, *ACS applied materials & interfaces* **2018** , 10, 25446; b) J. Zhou, M. Xie, F. Wu, Y. Mei, Y. Hao, R. Huang, G. Wei, A. Liu, L. Li, R. Chen, *Advanced Materials* **2021** , 33, 2101649; c) Z. Xu, S. Jin, N. Zhang, W. Deng, M. H. Seo, X. Wang, *Nano Letters* **2022** , 22, 1350; d) P. Liu, Z. Zhang, R. Hao, Y. Huang, W. Liu, Y. Tan, P. Li, J. Yan, K. Liu, *Chemical Engineering Journal* **2021** , 403, 126425.
- [10] a) W. Guo, Y. Zhang, X. Tong, X. Wang, L. Zhang, X. Xia, J. Tu, *Materials Today Energy* **2021** , 20, 100675; b) P. Xiao, H. Li, J. Fu, C. Zeng, Y. Zhao, T. Zhai, H. Li, *Energy & Environmental Science* **2022** , 15, 1638.
- [11] a) C. Liu, Z. Luo, W. Deng, W. Wei, L. Chen, A. Pan, J. Ma, C. Wang, L. Zhu, L. Xie, *ACS Energy Letters* **2021** , 6, 675; b) Y. Wang, Y. Chen, W. Liu, X. Ni, P. Qing, Q. Zhao, W. Wei, X. Ji, J. Ma, L.

- Chen, *Journal of Materials Chemistry A* **2021** , 9, 8452.
- [12] a) Q. Jian, Y. Wan, Y. Lin, M. Ni, M. Wu, T. Zhao, *ACS Applied Materials & Interfaces* **2021** , 13, 52659; b) X. He, Y. Cui, Y. Qian, Y. Wu, H. Ling, H. Zhang, X.-Y. Kong, Y. Zhao, M. Xue, L. Jiang, *Journal of the American Chemical Society* **2022** , 144, 11168; c) P. Chen, X. Yuan, Y. Xia, Y. Zhang, L. Fu, L. Liu, N. Yu, Q. Huang, B. Wang, X. Hu, *Advanced Science* **2021** , 8, 2100309; d) J. Hao, X. Li, S. Zhang, F. Yang, X. Zeng, S. Zhang, G. Bo, C. Wang, Z. Guo, *Advanced Functional Materials* **2020** , 30, 2001263.
- [13] L. Kang, M. Cui, F. Jiang, Y. Gao, H. Luo, J. Liu, W. Liang, C. Zhi, *Advanced Energy Materials* **2018** , 8, 1801090.
- [14] Q. Zhang, J. Luan, X. Huang, Q. Wang, D. Sun, Y. Tang, X. Ji, H. Wang, *Nature Communications* **2020** , 11, 3961.
- [15] P. Liang, J. Yi, X. Liu, K. Wu, Z. Wang, J. Cui, Y. Liu, Y. Wang, Y. Xia, J. Zhang, *Advanced Functional Materials* **2020** , 30, 1908528.
- [16] M. Gopalakrishnan, S. Ganesan, M. T. Nguyen, T. Yonezawa, S. Praserttham, R. Pornprasertsuk, S. Kheawhom, *Chemical Engineering Journal* **2023** , 457, 141334.
- [17] X. Pu, B. Jiang, X. Wang, W. Liu, L. Dong, F. Kang, C. Xu, *Nano-Micro Letters* **2020** , 12, 1.
- [18] M. Liu, L. Yang, H. Liu, A. Amine, Q. Zhao, Y. Song, J. Yang, K. Wang, F. Pan, *ACS applied materials & interfaces* **2019** , 11, 32046.
- [19] W. Xin, J. Xiao, J. Li, L. Zhang, H. Peng, Z. Yan, Z. Zhu, *Energy Storage Materials* **2023** , 56, 76.
- [20] H. Yang, Z. Chang, Y. Qiao, H. Deng, X. Mu, P. He, H. Zhou, *Angewandte Chemie* **2020** , 132, 9463.
- [21] W. He, T. Gu, X. Xu, S. Zuo, J. Shen, J. Liu, M. Zhu, *ACS Applied Materials & Interfaces* **2022** , 14, 40031.
- [22] a) M. Cui, B. Yan, F. Mo, X. Wang, Y. Huang, J. Fan, C. Zhi, H. Li, *Chemical Engineering Journal* **2022** , 434, 134688; b) X. Zeng, J. Zhao, Z. Wan, W. Jiang, M. Ling, L. Yan, C. Liang, *The Journal of Physical Chemistry Letters* **2021** , 12, 9055; c) X. Liu, F. Yang, W. Xu, Y. Zeng, J. He, X. Lu, *Advanced Science* **2020** , 7, 2002173.
- [23] Z. Wang, H. Chen, H. Wang, W. Huang, H. Li, F. Pan, *ACS Energy Letters* **2022** , 7, 4168.
- [24] F. Wang, H. Lu, H. Li, J. Li, L. Wang, D. Han, J. Gao, C. Geng, C. Cui, Z. Zhang, *Energy Storage Materials* **2022** , 50, 641.
- [25] H. Sun, Y. Huyan, N. Li, D. Lei, H. Liu, W. Hua, C. Wei, F. Kang, J.-G. Wang, *Nano Letters* **2023** , 23, 1726.
- [26] Y. Xiang, L. Zhou, P. Tan, S. Dai, Y. Wang, S. Bao, Y. Lu, Y. Jiang, M. Xu, X. Zhang, *ACS nano* **2023** .
- [27] D. Xu, X. Ren, Y. Xu, Y. Wang, S. Zhang, B. Chen, Z. Chang, A. Pan, H. Zhou, *Advanced Science* **2023** , 10, 2303773.
- [28] Y. Peng, Y. Li, Y. Ban, H. Jin, W. Jiao, X. Liu, W. Yang, *Science* **2014** , 346, 1356.
- [29] H. Ma, J. Yu, M. Chen, X. Han, J. Chen, B. Liu, S. Shi, *Advanced Functional Materials* **2023** , 2307384.
- [30] Y. Li, L. Lin, M. Tu, P. Nian, A. J. Howarth, O. K. Farha, J. Qiu, X. Zhang, *Nano Research* **2018** , 11, 1850.
- [31] W. Li, P. Su, Z. Li, Z. Xu, F. Wang, H. Ou, J. Zhang, G. Zhang, E. Zeng, *Nature communications* **2017** , 8, 406.
- [32] X. Yu, Z. Li, X. Wu, H. Zhang, Q. Zhao, H. Liang, H. Wang, D. Chao, F. Wang, Y. Qiao, *Joule* **2023** .

- [33] a) X. Zhou, Q. Zhang, Z. Zhu, Y. Cai, H. Li, F. Li, *Angewandte Chemie* **2022** , 134, e202205045; b) Q. Jian, Y. Wan, J. Sun, M. Wu, T. Zhao, *Journal of Materials Chemistry A***2020** , 8, 20175; c) R. Wang, M. Yao, M. Yang, J. Zhu, J. Chen, Z. Niu, *Proceedings of the National Academy of Sciences***2023** , 120, e2221980120; d) X. Xie, S. Liang, J. Gao, S. Guo, J. Guo, C. Wang, G. Xu, X. Wu, G. Chen, J. Zhou, *Energy & Environmental Science* **2020** , 13, 503.
- [34] Z. Zhao, J. Zhao, Z. Hu, J. Li, J. Li, Y. Zhang, C. Wang, G. Cui, *Energy & Environmental Science* **2019** , 12, 1938.
- [35] a) L. Hong, L. Y. Wang, Y. Wang, X. Wu, W. Huang, Y. Zhou, K. X. Wang, J. S. Chen, *Advanced Science* **2022** , 9, 2104866; b) Q. Jian, T. Wang, J. Sun, B. Liu, T. Zhao, *Chemical Engineering Journal* **2023** , 466, 143189.
- [36] a) M. Qiu, H. Jia, C. Lan, H. Liu, S. Fu, *Energy Storage Materials* **2022** , 45, 1175; b) Y. Yang, C. Liu, Z. Lv, H. Yang, Y. Zhang, M. Ye, L. Chen, J. Zhao, C. C. Li, *Advanced Materials***2021** , 33, 2007388.
- [37] W. W. Rudolph, C. C. Pye, *Physical Chemistry Chemical Physics* **1999** , 1, 4583.